DISCLAIMER

This report was prepared as an account of work sponsored by an agency of the United States Government. Neither the United States Government nor any agency thereof, nor any of their employees, makes any warranty, express or implied, or assumes any legal liability or responsibility for the accuracy, completeness, or usefulness of any information, apparatus, product, or process disclosed, or represents that its use would not infringe privately owned rights. Reference herein to any specific commercial product, process, or service by trade name, trademark, manufacturer, or otherwise does not necessarily constitute or imply its endorsement, recommendation, or favoring by the United States Government or any agency thereof. The views and opinions of authors expressed herein do not necessarily state or reflect those of the United States Government or any agency thereof. Reference herein to any social initiative (including but not limited to Diversity, Equity, and Inclusion (DEI); Community Benefits Plans (CBP); Justice 40; etc.) is made by the Author independent of any current requirement by the United States Government and does not constitute or imply endorsement, recommendation, or support by the United States Government or any agency thereof.

This document is the Final Report for:

U.S. Department of Energy
University Turbine Systems Research Program
Award Number: DE-FE0031806

DEVELOPMENT AND EVALUATION OF A NOVEL FUEL INJECTOR DESIGN METHOD USING HYBRID-ADDITIVE MANUFACTURING

Submitted to:
U.S. Department of Energy
National Energy Technology Laboratory
Point of Contact: Mark Freeman
Phone: 304-285-4185

Submitted by:
The Pennsylvania State University
University Park, PA 16802

Principal Investigator: Jacqueline A. O'Connor
Co-Principle Investigators: Guha Manogharan, Yuan Xuan
Department of Mechanical Engineering
Pennsylvania State University
University Park, PA 16802
Phone: (814) 863-1502
FAX: (814) 865-3389
Email: jxo22@psu.edu

Jacqueline O'Connor

Date: December 30, 2024

Program information

UEI: NPM2J7MSCF61

Recipient Organization: The Pennsylvania State University

Project Period: October 1, 2019 to September 30, 2024

Table of Contents

1 Executive Summary

The widespread application of metal additive manufacturing (AM) technologies has enabled exploration of complex design spaces to achieve optimally performing components. Current optimization techniques make use of several advanced methods to provide designs that are superior to existing versions. However, they seldom discuss the manufacturability of the optimal designs. The objective of this project was to develop a design optimization tool that simultaneously optimizes fuel injector hardware and the combustor flow field with optimization functions and constraints that consider both combustor performance and manufacturability using advanced AM methods and post-processing. In this way, the resultant hardware design is inherently imbued with our most advanced knowledge of combustion physics and AM methods from its conception.

The optimization process developed as part of this grant simultaneously integrates optimization for combustion performance, particularly fuel flexibility with hydrogen, and design for addivite manufacturing (DfAM) principles. During a standard adjoint shape optimization routine, there is limited provision in current commercial solvers to impose geometric constraints while deforming the mesh. Therefore, to simultaneously optimize fluid flow using the multi-physics adjoint while imposing DfAM constraints, augmentation of the standard adjoint shape optimization routine was implemented. After computing the shape sensitivities in commercial computational fluid dynamics (CFD) software of the adjoint shape optimization routine, the shape sensitivities along with the control point locations were exported from the CFD software. These shape sensitivities, combined with the defined step size, provide displacement vectors which were used to modify the shape parametric data externally and obtain a modified geometry. Since the modification is performed externally, the DfAM constraints can be incorporated as a design operation followed by re-inserting the modified design into the CFD adjoint shape optimization loop.

There were six main learning outcomes of the project. First, we achieved integration of design for AM and combustion behaviors into an optimization routine to design gas turbine fuel injectors for for fuel-flexible operation. Second, this was done using commercial tools and open-source resources (Python code, standard CAD definitions, etc.) to implement optimization for better translation to industry and other researchers. Third, the AM optimization was based on a mathematical formulation rather than grid-based, allowing better transference to other applications than just fuel injectors. Fourth, research during this grant led to better understanding of the role of pilot jets in flow stability and flameholding, which was critical to the design of industrial fuel injectors. Fifth, we developed new understanding of the impact of AM surface roughness on flameholding. Finally, we designed and tested both optimized injector designs and clean-sheet designed based on lessons learned from the optimization process. These injectors were tested in simulation and in experiments.

2 Project Overview

2.1 Project Goals

The objective of this project was to develop a design optimization tool that simultaneously optimizes fuel injector hardware and the combustor flow field with optimization functions and constraints that consider both combustor performance and manufacturability using advanced AM methods and post-processing. In this way, the resultant hardware design is inherently imbued with our most advanced knowledge of combustion physics and AM methods from its conception. This project will be executed in close collaboration with Solar Turbines, the industry cost-share partner. Engineers at Solar will work extensively with the team of professors and students at Penn State in the areas of manufacturing methods, combustion simulation, and overall combustion design. The result of this partnership will be a design tool that can be integrated into current standard design practices in industry and could radically reshape the design space for this critical yet historically complex hot-section component. These methods could be also be extended to other hot-section components where multi-disciplinary optimization is required, including combustor transition pieces, turbine nozzle vanes, and potentially even turbine blades.

2.2 Project Approach

2.2.1 Partners

The industrial partner for this grant was Solar Turbines, who provided technical expertise as well as cost share for the program. Throughout the program, researchers at Penn State worked closely with engineers at Solar Turbines to determine the course of the program on issues related to combustion simulation, additive manufacturing, and design optimization. Results from the project were reported to Solar Turbines engineers and leadership at bi-annual Center of Excellence meetings, where a broader audience of Solar Turbines employees could provide feedback on the program. Additionally, representatives from Solar Turbines often attended the yearly UTSR program reviews, providing another avenue for interaction and feedback.

Penn State researchers worked closely with partners at the Indian Institute of Science – Bangalore (IISc), particularly Professor Santosh Hemchandra, associate professor of Aerospace Engineering, on issues related to flow stability. The team licensed a flow stability prediction tool called FEHydro from partners at IISc, which was used to understand the impact of design changes on the hydrodynamic stability of the flow from the fuel injector, which has significant implications for flame stability.

Finally, the PIs and their students worked closely with researchers at Center for Innovative Materials Processing through Direct Digital Deposition (CIMP-3D), the additive manufacturing center operated jointly by the Penn State College of Engineering and the Penn State Applied Research Laboratory. Researchers at CIMP-3D helped with setup and execution of the injector printing.

2.2.2 Computational Methods

The various injector designs investigated in this project were first integrated into the full test rig CAD file and then imported into the StarCCM+ software for Computational Fluid Dynamics (CFD) simulations. A typical CAD model of the full rig is shown in Figure 1.

Figure 1. Typical test rig CAD file imported into StarCCM+.

The combustor liner and centerbody of the injector were typically maintained at 900 K and 600 K, as they were heated by the prolonged impingement of the flame. Elsewhere, the walls were assumed to be adiabatic. These simulation boundary conditions are derived from previous experiments conducted on this rig [1]. The incoming air was typically preheated to 523 K with a bulk velocity in the main channel of 40.65 m/s across all fuel composition and equivalence ratios to match experimental conditions.

We primarily used Large-Eddy Simulations (LES) as the CFD modeling framework in this project, in combination with some Reynolds Averaged Navier-Stokes (RANS) simulations. The low-Mach number (incompressible limit) LES approach was used in StarCCM, where Favre-averaged conservation equations were solved with dynamic Smagorinsky based sub-grid scale models. When RANS was employed, we used the two-equation $k - \omega$ shear stress transport (SST) model for turbulence modeling.

The Flamelet-Generated Manifold (FGM) method was used for turbulent combustion modeling, for its accuracy and computational efficiency. In FGM, all relevant thermochemical variables were tabulated as functions of species-weighted progress variable, mixture fraction, and local heat loss according to a large number of pre-computed 1D freely propagating premixed flamelet solutions. Then, the transport equations for these three flamelet variables were solved in LES to predict the spatial and temporal distributions of the thermochemical states in the test rig. A Turbulent Flame Speed Closure (TFSC) model was also used to provide the source term in the transport equation of the progress variable. Therein, the algebraic model of turbulent flame speed from Zimont et al. [2] was used, since it accounts for the effects of flame stretch and wall quenching.

The GRI Mech 3.0 and USC Mech II were typically used as the chemical kinetics mechanisms to generate the FGM table for LES or RANS simulations. GRI Mech 3.0 encompasses 325 elementary chemical reactions, along with their corresponding rate coefficient expressions and thermochemical parameters, for a total of 53 species. This mechanism operates effectively within a temperature range of 1000–2500 K, a pressure range of 10 torr–10 atm, and equivalence ratios between 0.1 and 5.0. It contains a detailed combustion reaction mechanism for hydrogen. USC Mech II is a model detailed chemical kinetic model, consisting of 111 species and 784 elementary reactions. Developed by the University of Southern California in 2007, this model can simulate the oxidation of hydrogen, carbon monoxide, and C1–C4 hydrocarbons at high temperatures.

The polyhedral mesher, prism layer mesher, and surface remesher were executed in parallel mode to generate the computational mesh within StarCCM+. The polyhedral mesher was used to build the core mesh in arbitrary polyhedral cell shape. The advantages of polyhedral mesher are (1) faster convergence with fewer iterations; (2) robust convergence to lower residual values; (3) faster solution runtimes. The base cell size of the core mesh was chosen as 3mm. The core mesh resolution (base cell size) in different parts of the test rig were adjusted separately. For example, the base cell size in the combustor was typically set as 30% of base size (0.9 mm). In general, the mesh resolution in the injector and combustor was usually higher than those in the inlet and exhaust because of the high velocity fluctuation and heat release fluctuations. The prism layer mesher was used to generate orthogonal prismatic cells next to the wall or domain boundaries. The prism layer stretching ratio was set to be 1.5. A total of 5 prism layers were implemented in all mesh settings for a smoother transition from the walls to the core mesh. In addition, to accommodate the different base cell sizes in the injector and combustor, the total prism layer thickness was also adjusted for a smoother transition from boundaries to the core mesh cell. The surface remesher was chosen to re-triangulate the surface which can improve the mesh quality of a surface and optimize it for the volume mesh models.

We carried out convergence studies to determine the optimal mesh settings which can achieve sufficient accuracy without excessive computational cost. The convergence test matrix is shown in Table 1. For all mesh tests, the reference base size was chosen as 3 mm. The base cell size in the injector and combustor were systematically reduced from 100% to 50%, 35%, 30%, 20% of the reference base size, since the flow is only expected to have important small-scale features in these two parts of the entire rig. The base sizes in the injector and combustor were not reduced further because of the considerable increase in computational cost. The cell sizes in the inlet, settling chamber, and exhaust were kept the same as 100% of the reference base size. The total number of cells in the entire rig varied from 2.49 million to 16.6 million in the mesh convergence test matrix. It was observed that mesh convergence was achieved with injector and combustor cell sizes smaller than 30% of the base size. Therefore, the spatial resolution of the fourth mesh in the test matrix below was used for all LES and RANS simulations in this project. Similarly, the optimal time step size in unsteady LES and RANS simulations was determined to be 5e-5s in a temporal convergence study.

Table 1. Mesh convergence test matrix.

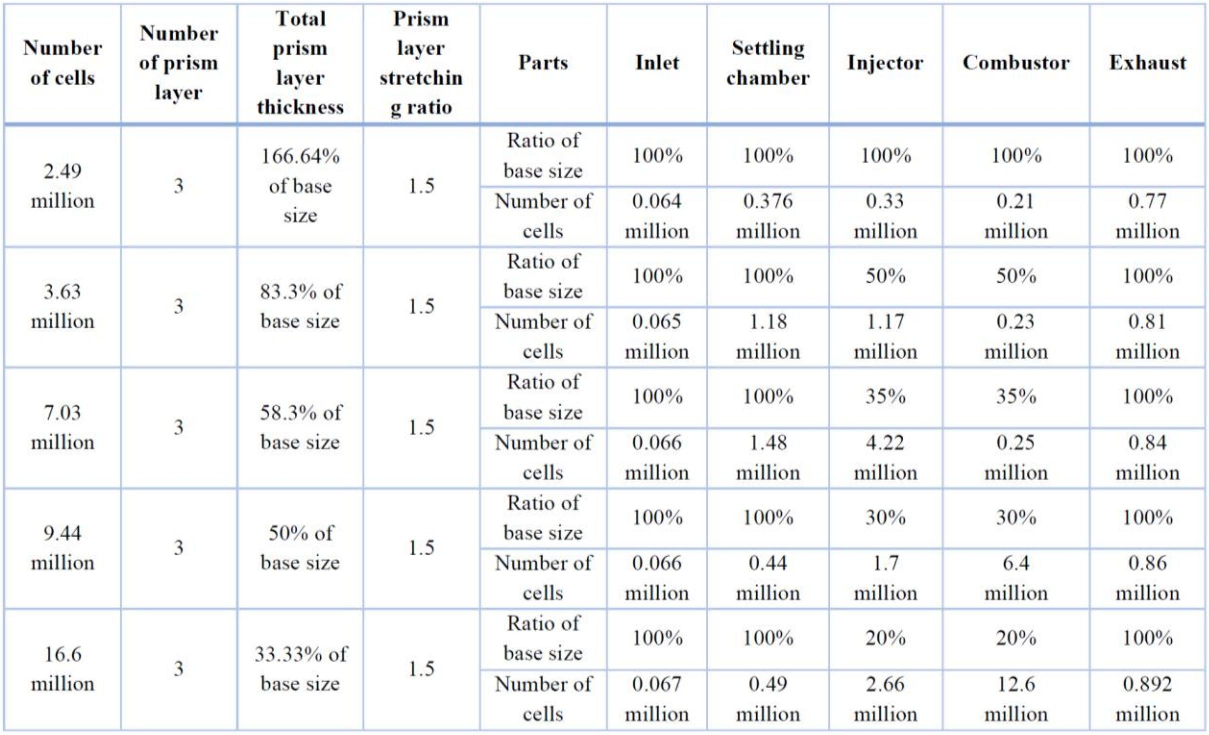

Number of cells	Number of prism layer	Total prism layer thickness	Prism layer stretching ratio	Parts	Inlet	Settling chamber	Injector	Combustor	Exhaust
2.49 million	3	166.64% of base size	1.5	Ratio of base size	100%	100%	100%	100%	100%
				Number of cells	0.064 million	0.376 million	0.33 million	0.21 million	0.77 million
3.63 million	3	83.3% of base size	1.5	Ratio of base size	100%	100%	50%	50%	100%
				Number of cells	0.065 million	1.18 million	1.17 million	0.23 million	0.81 million
7.03 million	3	58.3% of base size	1.5	Ratio of base size	100%	100%	35%	35%	100%
				Number of cells	0.066 million	1.48 million	4.22 million	0.25 million	0.84 million
9.44 million	3	50% of base size	1.5	Ratio of base size	100%	100%	30%	30%	100%
				Number of cells	0.066 million	0.44 million	1.7 million	6.4 million	0.86 million
16.6 million	3	33.33% of base size	1.5	Ratio of base size	100%	100%	20%	20%	100%
				Number of cells	0.067 million	0.49 million	2.66 million	12.6 million	0.892 million

2.2.3 Experimental Methods

Experiments are carried out in a single-nozzle, optically accessible combustor. As shown in Figure 2, the combustor consists of an inlet section, an optically-accessible quartz liner, and a variable-length metallic section. The quartz combustor liner has a 15 cm diameter and 30.5 cm length, and allows the entire structure of the flame to be accessed optically. Several different injectors were tested in the same experiment, including the baseline industrial injector and a range of additively manufactured injectors. Each injector had the same outer diameter and length such that it could be easily swapped into the experiment for testing.

The quartz combustor liner is coupled to a 12.3 cm inner diameter variable-length metallic section containing a water-cooled plug. A stepper motor-controlled traverser system (Isel-Automation) allows the overall combustor length between the dump plane and the water-cooled plug to be varied between 63.5-149.9 cm in increments of 0.25 cm, although all the analysis described in this paper was done at a combustor length of 63.5 cm. Figure 3 shows an image of the experiment.

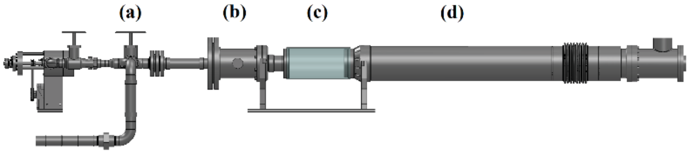

Figure 2: The experimental apparatus showing: a) the inlet section; b) the plenum; c) the quartz combustor; and d) the metallic variable-length combustor.

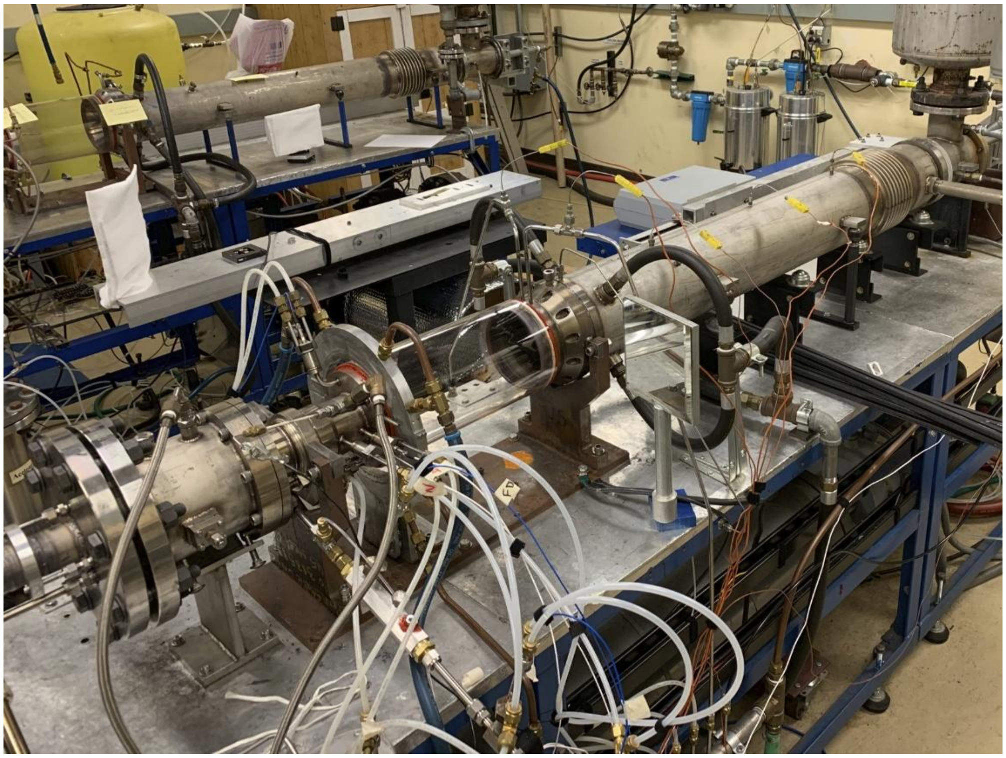

Figure 3. Single-nozzle combustion facility.

2.3 Project Modification

A two-year no-cost extension was obtained in FY2022 due to several factors. First, hiring students at the beginning of the project took longer than initially expected and the second funded student didn't start until almost nine months into the start of the project. Second, the COVID-19 pandemic significantly disrupted operations on the project for both graduate students and PIs, resulting in significant delays to project progress. Finally, one of the initial graduate students on the project left graduate school early and so a personnel change was required at the end of FY2022 and a new student was on-boarded.

A significant modification of project objectives occurred in the fourth quarter of FY2023 due to both the prior delays and initial findings of the project. The tasks were updated in the Project Management Plan, resulting in the final task list outlined in Table 2.

Table 2. Modified task list at the end of FY2023.

Task	Description	Target Date
1.0	**Project management and planning**	n/a
2.0	**Establish baseline**	9/30/2020
2.1	Identify baseline fuel injector geometry	12/31/2019
2.2	Design mapping	3/31/2020
2.3	Operational mapping – experiment	3/31/2020
2.4	Operational mapping – simulation	3/31/2020
2.5	Stability mapping – LHSA	3/31/2020
2.6	Design and fabricate new test facility	9/30/2020
3.0	**Develop design optimization tool**	9/30/2020
3.1	Identify optimization parameters and constraints	9/30/2020
3.2	Integrate optimization functions	9/30/2020
4.0	**Implement optimized design process – baseline**	6/30/2021
4.1	Apply optimization to baseline	3/31/2021
4.2	AM design	12/31/2023
4.3	Simulation and stability of new design	6/30/2024
4.4	Print new design	12/31/2023
4.5	Test new design in experiment	9/30/2024
4.6	Evaluation of Task 4 Results	9/30/2024
5.0	**Evaluation of AM Constraints**	9/30/2024
5.1	Evaluation of geometric constraints	9/30/2023
5.2	Evaluation of build constraints	12/31/2023
6.0	**Evaluation of Combustion Behaviors**	9/30/2024
6.1	Impact of design of flow stability – non-reacting	9/30/2023
6.2	Impact of design on flow stability – reacting	3/31/2024
6.3	Impact of fuel composition on flame stability	9/30/2024
7.0	**Final process testing and technology transfer**	9/30/2024
7.1	Technology transfer	9/30/2024

3 Project Accomplishments and Results

3.1 Development of Design Optimization Methodology for AM and Combustion Behaviors

This part of the project includes three main accomplishments related to the integration of Design for Additive Manufacturing (DfAM) principles and optimization for combustion behaviors:

- Development of a method for defining surface geometries that can be optimized for both DfAM and fluid mechanic and combustion behaviors
- Development of a method for shape optimization linking DfAM and commercial CFD solvers
- Development and testing of the final optimization methodology

Overviews of these three accomplishments are provided here. Corresponding publications are identified in each of the subsections.

3.1.1 Development of geometry definition methodologies

This work has been submitted for publication and is currently under review; the following section provides an overview of this work. The final publication will be uploaded to OSTI when available.

The widespread application of metal additive manufacturing (AM) technologies has enabled exploration of complex design spaces to achieve optimally performing components. Current optimization techniques make use of several advanced methods, such as adjoint shape optimization, to provide designs that are superior to existing versions. However, they seldom discuss the manufacturability of the optimal designs. This research introduces novel restrictive design for AM (DfAM) constraints through computer-aided design (CAD) file modification, which were used to guide the adjoint shape optimization process. The baseline design, using an application of a gas turbine fuel injector, was parameterized using non-uniform rational B-splines (NURBS) surface information stored in standard initial graphics exchange specification (IGES) file format. Gradient information computed using a commercial computational fluid dynamics (CFD) solver was used for NURBS shape modification in Python while focusing on imposing overhang angle and thin wall constraints for metal-AM. A method was developed to selectively replace information in the IGES file to accommodate modified design of surfaces of interest while preserving the overall geometry and maintain file integrity. The framework accounts for varying levels of design complexity, accepting gradient information from commercial simulation software while imposing user-defined metal-AM constraints to obtain an optimal, additively manufacturable design. Findings from this study can be readily implemented in DfAM of any surface fluidic devices produced via metal laser AM, specifically Laser-Powder Bed Fusion.

An overview of the integration of NURBS-based restrictive DfAM constraints into the optimization process is provided in Figure 4. The process began with parameterization of the swirler vanes to a CAD format with NURBS-readable data. In doing so, many strategies were used to ensure continuity and coherence of the shape definition of the part. The NURBS parametric data was then read using in-house developed Python code. The parametric data extracted from the CAD file was then modified using imported adjoint data from Star-CCM+ and imposing overhang angle and thin wall constraints. The modified data was replaced in the original CAD file and preserved for formatting. Details of this process are provided in the manuscript, which will be uploaded to OSTI when available.

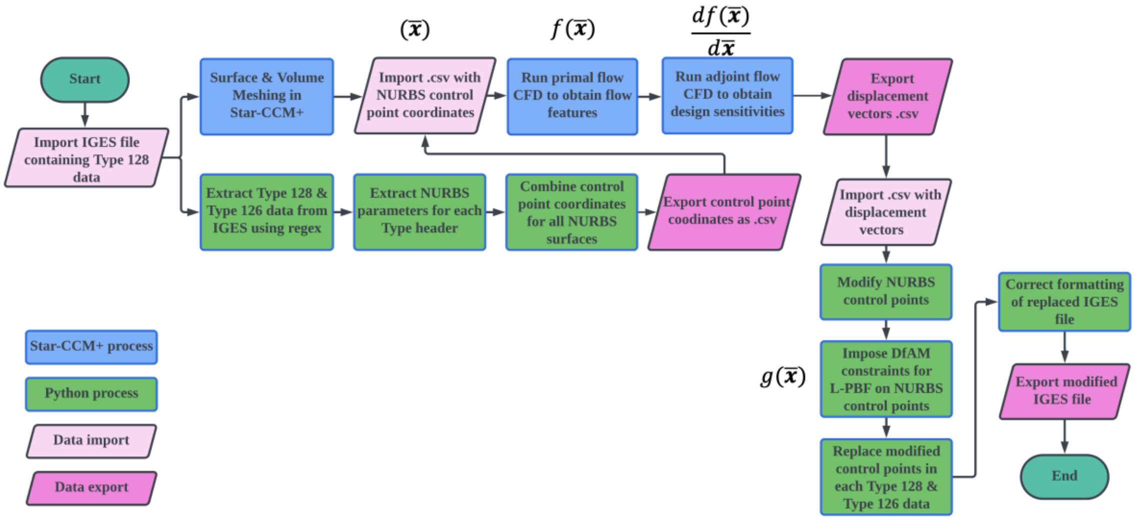

Figure 4: Summary of the NURBS-based adjoint shape optimization framework

The modified geometry was suitable for self-supporting printing but changing the shape led to changes in the anticipated performance of the part. Just by changing the shape to meet DfAM self-supporting constraints, a 15% higher objective function value of volume averaged velocity magnitude in the turbulent boundary layer region near the combustor exit was observed. The effect of the shape changes on the performance of the fuel injector using reacting simulations is a part of ongoing and future research which includes simulation and fabrication of the baseline, DfAM, and flashback optimized fuel injectors which are undergoing combustion tested to obtain experimental comparisons in performance.

3.1.2 Development of shape optimization methodologies

This work has been published open-access in: Jalui, S., Xuan, Y., Manogharan, G., and O'Connor, J. (October 15, 2024). "Development of a Method for Shape Optimization for a Gas Turbine Fuel Injector Design Using Metal-Additive Manufacturing." *ASME. J. Eng. Gas Turbines Power*. January 2025; **147**(1): 011023. https://doi.org/10.1115/1.4066509. The author-accepted version of this paper has also been uploaded to OSTI. An overview of the results are provided here.

The objective of this study was to develop a method to enable simultaneous optimization of flow fields using the adjoint method and impose Design for Additive Manufacturing (DfAM) constraints. This goal was achieved by modifying a commercial CFD optimization routine that used an adjoint method to modify an injector geometry with both flow constraints (inside the CFD optimization) and DfAM constraints (outside the CFD solver), which are currently not available for implementation in commercial solvers. These two methods used different geometry definitions for the injector shape, making the focus of this work to ensure consistency between the optimization routines, where the commercially available CFD routine uses RBF-interpolated surfaces and the DfAM optimizer uses a NURBS-interpolated surface. The differences between these definitions must be maintained within the AM L-PBF process tolerances to justify the use of these methods together. This work was motivated by the need to adopt DfAM optimization more widely and integrate it with commercial software. This work used StarCCM+ 2021.3 as an example commercial software, as it is widely used in the gas turbine industry. The optimization process consists of six steps, the details of which are provided in the open-access manuscript:

1. Defining the design variables
2. Meshing the flow region
3. Solving for the primal solution in the CFD solver
4. Solving for the adjoint solution in the CFD solver

5. Using the adjoint to compute mesh sensitivity to a flow optimization criterion
6. Deforming the mesh outside the CFD solver within the constraints of the DfAM parameters

In this study, the process was fully automated and the sensitivity to step size in the optimization process was analyzed. Details of the CAD modification for DfAM optimization is described in detail in the open-access manuscript. The method was tested on a simple airfoil geometry to optimize lift coefficient to show the utility of this method on a well-established aerodynamic problem. After showing the results of the functioning method on a simple geometry, a swirler-based fuel injector was optimized for both flashback performance and DfAM constraints. For full results, see the open-access publication.

3.2 Understanding the Role of Pilot Jets in Flameholding and Flow Stability

The results of this part of the study were published in the following manuscript: Li, J., Kwon, H., Seksinsky, D., Doleiden, D., O'Connor, J., Xuan, Y., Akiki, M., and Blust, J. (October 18, 2021). "Describing the Mechanism of Instability Suppression Using a Central Pilot Flame With Coupled Experiments and Simulations." *ASME. J. Eng. Gas Turbines Power*. January 2022; **144**(1): 011015. https://doi.org/10.1115/1.4052384. This section provides an overview of the study.

Combustion instability is driven by the coupling between heat release rate oscillations and resonant combustor acoustics and is a significant issue for low-emissions gas turbine engines [3]. These unstable conditions are reached to prevent NOx emissions, which can be avoided by running at fuel-lean conditions where the flame is more susceptible to perturbations [4]. The focus of this study is to understand how the use of a central pilot flame, which is a common feature in industrial gas turbine engines, can suppress combustion instability in some cases.

This work is based off prior work by Li et al. [5] in this same experimental configuration, which showed a thermoacoustic stability map as a function of global equivalence ratio and pilot fuel flow rate. Without piloting, the flame was not well anchored and not stabile. Increasing pilot fuel flow rate could change the instability amplitude depending on the equivalence ratio of the pilot; if it was greater than that of the main flame, then it suppressed the instability, but if it was lower, then it could exacerbate it. More details of the original study are provided in the paper.

This prior work raised the question of how a pilot flame enhances flame stability, which is investigated in this study using high-fidelity large-eddy simulation (LES). Four cases from the original study are simulated and analyzed. The time-averaged flame shapes match well between experiment and simulation, and more detailed analysis of the thermochemical state throughout the combustor shows that back-support of the main flame by the pilot flame enhances both static and dynamic stability. More details of this analysis are provided in the paper.

3.3 Understanding the Impact of AM Surface Roughness on Flameholding

This work is being prepared for submission for publication; the following section provides an overview of this work. The final publication will be uploaded to OSTI when available.

This part of the study compared the shape and stability limits of a swirl-stabilized flame for smooth (cast) and rough (AM) fuel injectors using both simulation and experiments. Blends of hydrogen and natural gas are used to understand this manufacturing technology's impact on low-carbon fuel blends. The first goal of the work is to understand trends in flame stability with different roughness levels for a range of fuel blends and explain those trends using a combination of simulation and experiment. The simulations are done using Reynolds-averaged Navier-Stokes (RANS) methods with wall roughness models, mimicking the types of tools that would be used in industry. The second goal of the work is to test whether these tools can capture the same trends measured in experiments.

The as-built surface quality of a given geometry differs by regions based on the print orientation. With respect to the print orientation, AM surfaces are categorized and up-skin, down-skin, and vertical surfaces. Up-skin surfaces are those surfaces where the projection of the surface normal along the print direction is positive. The up-skin side of a given geometry has the best as-built surface quality since it is self-supported by the solidifed material from previous layers and the layers undergo re-melting, which provides more uniform energy application and heat distribution. Most of the contribution towards surface roughness is due to the staircasing effect of layerization on sloped and curved surfaces. Downward-facing surfaces have a negative surface normal projection along the build direction. These surfaces usually have the poorest as-built surface quality due to complex interactions between the laser and surrounding powder and the need for support structures. They are prone to accumulation of thermal stresses, which may cause thermal distortion. The vertical surfaces have the surface normal perpendicular to the build direction and the as-build surface quality is a function of layer thickness and laser intensity and has an average value between the two extremes. These surface types of the current geometry are identified in Figure 5.

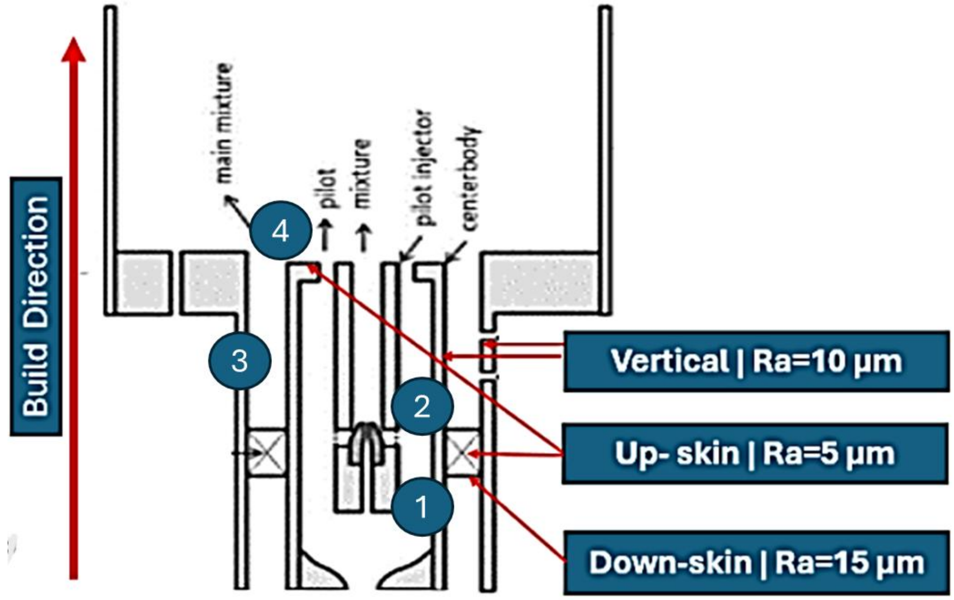

Figure 5. Schematic of injector and surface roughness levels on various surfaces.

The experiment is modeled to scale in Simcenter STARCCM+ as detailed in Section 2.2.2. The boundary conditions are set to mimic the experimental setup. The combustor liner and centerbody are maintained at 900 K and 600 K as these are heated due to prolonged impingement of the flame with extended operations; simulation boundary conditions are derived from previous experiments conducted on this rig. The incoming air is preheated to 523 K with a flow rate of 0.06 kg/s. The flow is split between a main and pilot circuit, where the pilot accounts for 5% pilot flow of the total flow. The fuel is perfectly premixed with the air, resulting in both a premixed main and premixed pilot flame. Premixing inlet condition was chosen to eliminate any effects of local equivalence ratio variation of the reactants and preserve only roughness effects on the flame. The bulk velocity in the main channel is maintained at ~40.65 m/s across all fuel composition and equivalence ratios to match experimental conditions.

An unstructured polyhedral non-adaptive mesh of a base cell size of 3 mm is initially auto-generated. The various regions of the rig CAD are meshed relative to the base size. The swirler and combustor region have the finest mesh settings of 30% of the base cell size. The swirler region is wall-resolved at $y^{+}_{wall}=1$ to accurately capture the sub-layer velocity distribution. The mesh has 11 prism layers with a total thickness of 2 mm (67% of the base mesh size) and a stretch ratio of 1.5. This thickness value is higher than the

Blasius approximation of turbulent boundary layer thickness in a flat channel, which is estimated as 1.37 mm. The remaining confined regions of the rig have a y^+_{wall} =17.6.

The turbulence is modeled using the k-ω shear stress transport (SST) Menter model in a steady-state RANS model. The SST k-ω version includes a non-conservative cross diffusion term, which is the blending function that allows for the application of this cross-diffusion component in freestreams away from the wall. Details of the chemistry model are provided in Section 2.2.2. The roughness is modeled using a blended wall velocity function that determines the relationship between normalized velocity, u^+, to normalize wall distance, y^+ [6]. The surface roughness modifies the the wall function by a factor, which impacts only in the log layer of the boundary layer. Initially, three levels of equivalent sand-grain wall roughness employed in the annulus duct of the injector (printed in vertical orientation) -- smooth, transitionally rough, and fully rough were simulated for 50% by vol. hydrogen in methane, at a $\phi = 0.58$ to understand the impact of the roughness on the velocity profile near the wall.

Figure 6 shows the non-dimensional velocity plotted against the non-dimensional wall distance, capturing the turbulent boundary layer profile on the inner main wall along the injector centerbody. An increase in the equivalent sand-grain roughness decreases the log-layer velocity. In the fully rough case, the viscous sublayer is fully destroyed and the near-wall velocity decreases in this region as well, indicating the potential for the turbulent flame to take advantage of such low-velocity regions for boundary wall flashback. For the case of the as-built injector roughness that lies in the transitional regime, the axial velocity in the viscous layer is slightly higher than in the smooth case. In quantitative terms, a maximum of 5% decrement is noted in the non-dimensional velocity from smooth to the transitionally rough case, and a reduction of 29.5% is observed for the fully rough case.

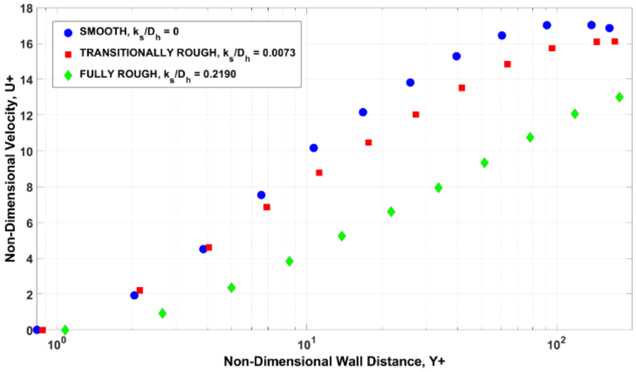

Figure 6. Non-dimensional boundary layer velocity profiles for three surface roughnesses.

This change in the boundary layer structure with wall roughness affects the flow profile and turbulence intensities downstream of the injector where the flame is stabilized. Figure 7 shows the radial profile of the axial velocity at various locations downstream of the dump plane for the three wall roughness cases. Increasing the surface roughness causes a higher peak velocity at several downstream locations and increases the width of the annular jet, resulting in a thinner vortex breakdown region. These changes to the flow profile are a direct result of the thickening of the boundary layer caused by the surface roughness, which decreases the effective area of the channel, increasing the peak velocity in the profile.

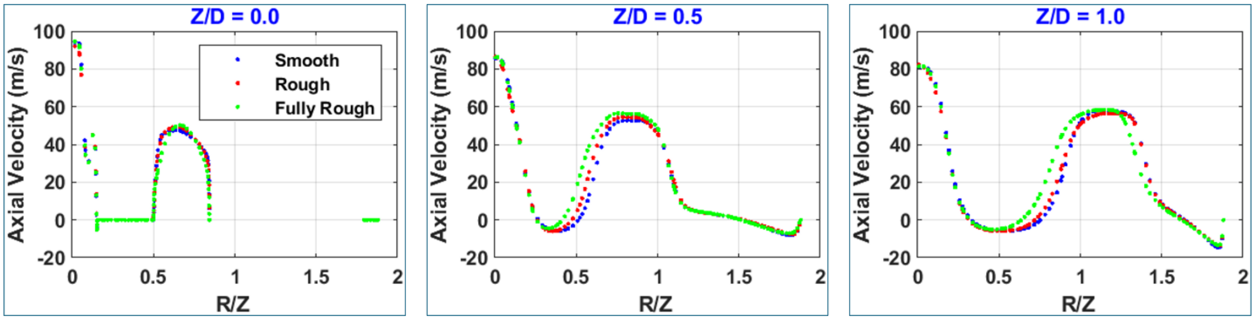

Figure 7. Axial velocity profiles as a function of radius for three downstream distances and three surface roughness levels.

Figure 8 shows the radial profile of the turbulence intensity at different downstream distances for the three surface roughness cases. The peak TI% increases with increasing roughness and the overall profile shifts inwards at each downstream location. Again, these results align with the change in the boundary layer in the channel, where the roughness causes thicker boundary layers and higher turbulence intensities ahead of the boundary-layer separation point, which results in higher turbulence intensities in the downstream shear layers. Similar results are obtained for all fuel compositions and equivalence ratios.

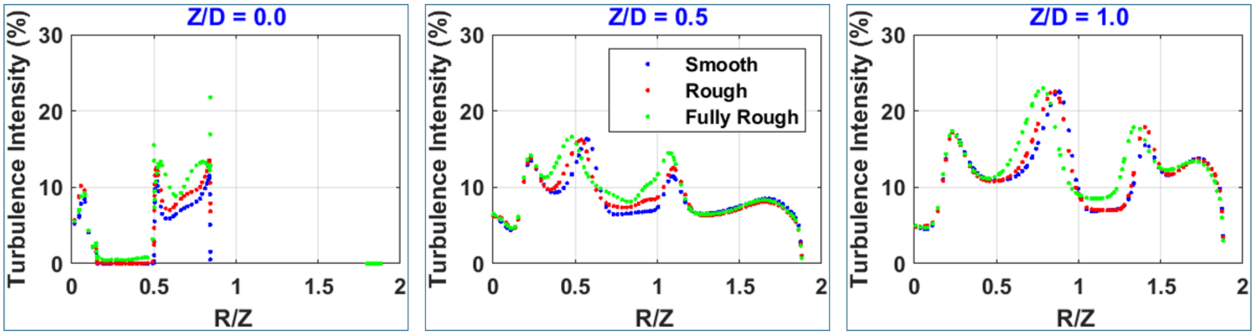

Figure 8. Turbulence intensity profiles as a function of radius for three downstream distances and three surface roughness levels.

Figure 9 presents the heat release rate profile and its iso-contour at 10% of the maximum heat release rate, depicted as a white line for each of the roughness cases, for an example case of 50% hydrogen enrichment and ϕ=0.58. The flame length is calculated as the distance from the centerbody edge to the tip of the 10% isocontour, marked with a white arrow in the bottom image. The reported flame length is an average of either side of the image. At this condition, the increase in surface roughness causes a decrease in the flame length. This decreasing flame length is due to increased turbulence in the vicinity of the dump plane, leading to faster consumption of the reactive mixture and higher turbulent flame speed. The flame length for the transitional rough case decreases by 6% with respect to the smooth case. For the hydraulically rough case, the decrease in flame length is 23%.

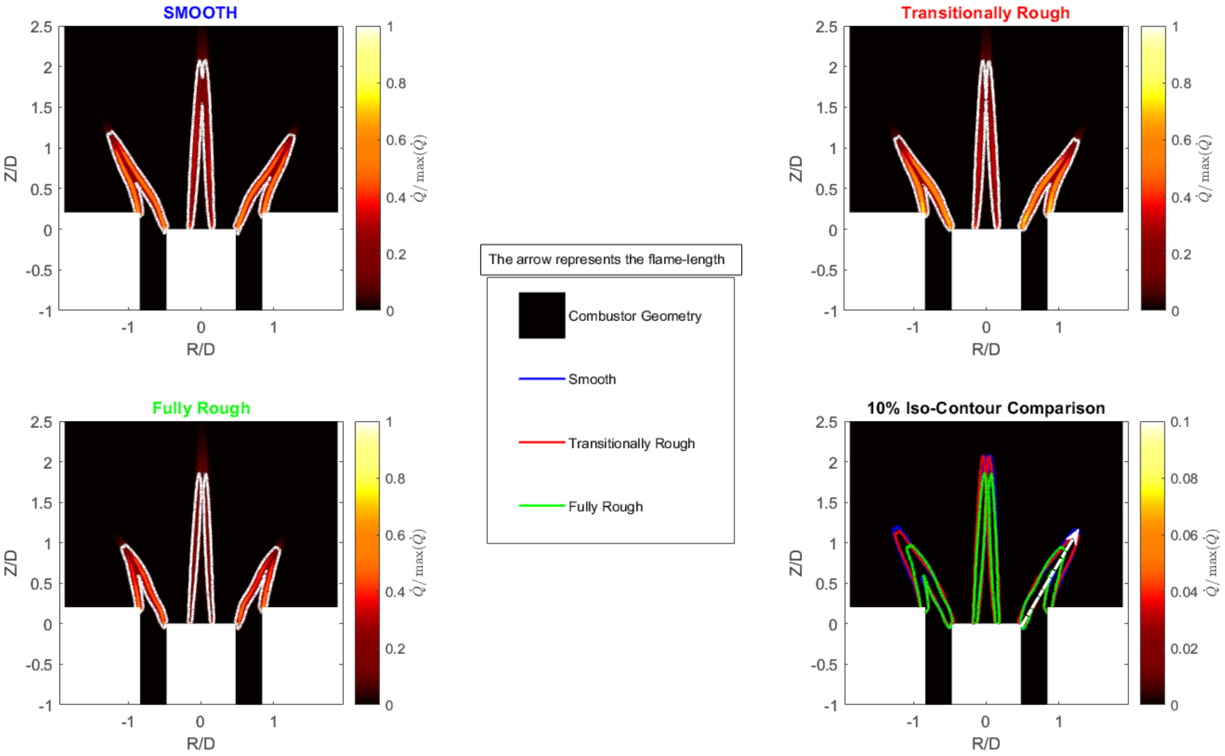

Figure 9. Heat release rate profiles with 10% isocontours for three surface roughness levels at 50% H_2.

Figure 10 shows the flame lengths for the two roughness cases as a function of hydrogen percentage in natural gas at a constant adiabatic flame temperature of 1840 K. The flame length decreases as the roughness level increases across all hydrogen levels due to the increased laminar flame speed of hydrogen. The flame length in the transitionally rough injector is 4% less than that of the smooth injector for hydrogen levels below 40%. At higher levels of hydrogen, the difference between the smooth and rough cases increases rapidly, where the transitionally rough case is 11% shorter than the smooth case for 60% hydrogen. At 70% hydrogen, the flame in the smooth injector stabilized inside the main channel instead on the centerbody edge. The rough injector flame tends to follow the decreasing flame length trend even at 70% enrichment. For the stated operating conditions of fuel composition and flow rate, both the injectors flashback at higher hydrogen levels, as can be seen in Figure 11.

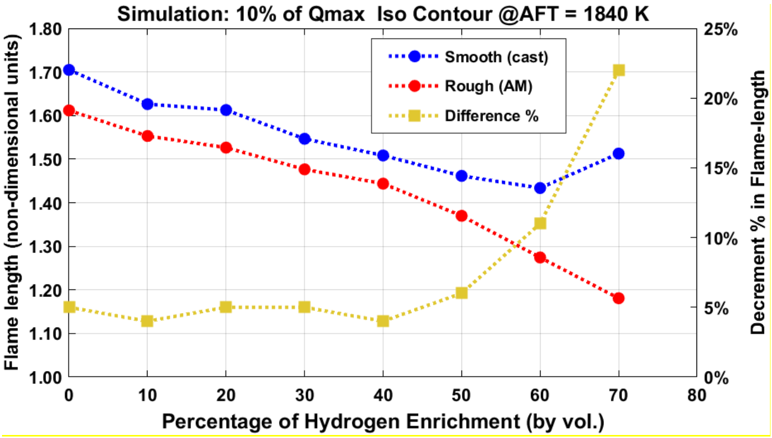

Figure 10. Flame length as a function of hydrogen level in the fuel for two surface roughness levels.

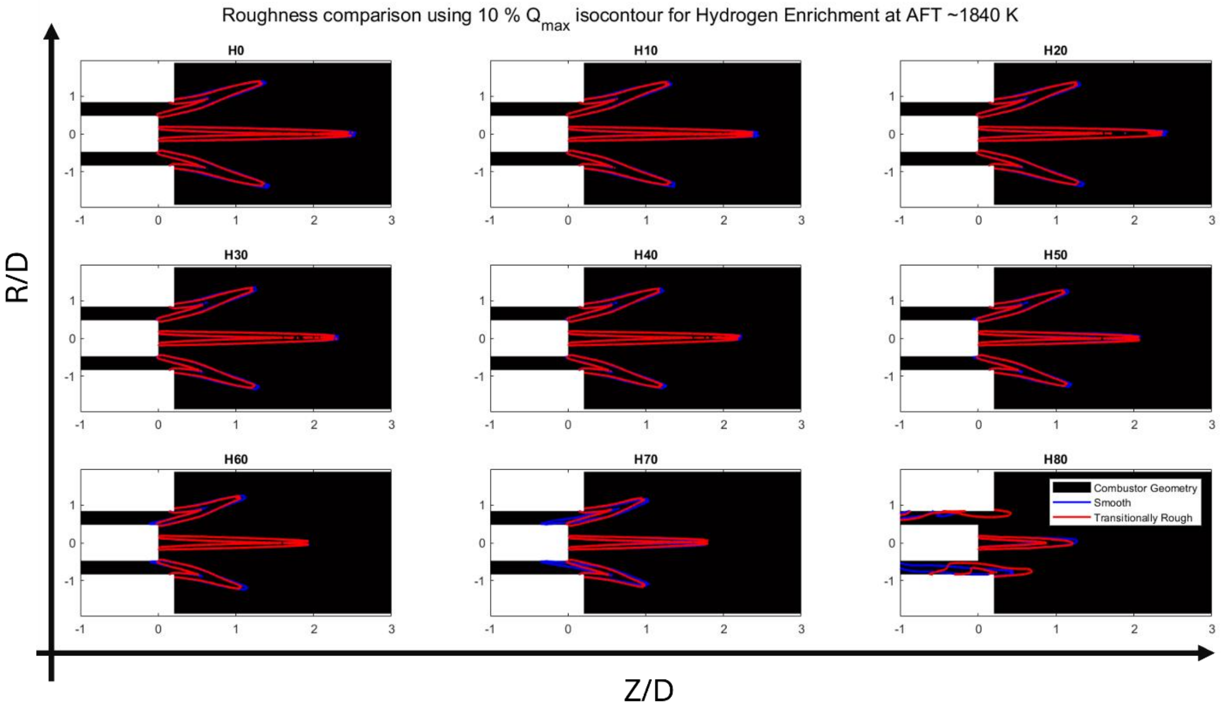

Figure 11. Flame shape for two roughness levels across all hydrogen levels.

As surface roughness changes the flame shape and stabilization, it would follow that it may also impact the flashback and blowoff limits of the flame. Figure 12 shows the flame length as a function of equivalence ratio for the smooth and transitionally rough cases as a function of equilvance ratio for five fuel blends. The data are recorded between the lean blowoff limit and the flashback limit. The secondary y-axis defines the percentage difference in the flame length between the two levels of roughness. With increasing hydrogen enrichment, the blowoff and flashback equivalence ratios decrease due to increasing laminar flame speed at each equivalence ratio, as would be expected for higher hydrogen flames. However, there are significant differences in the blowoff and flashback equivalence ratios between the two different levels of roughness.

In the pure methane case, the two roughness cases have the same operability limits, but the smooth injector has a longer flame near the blowoff limit than at the flashback limit. At the blowoff limit, the flame length in the rough injector is nearly 11% shorter. The difference is the lowest for ϕ=0.55 and then tends to increase again for the higher equivalence ratio cases by 8%. For the same range of equivalence ratio, in the case of 20% hydrogen, that difference in flame length almost doubles for ϕ=0.9.

The 40% hydrogen case is particularly interesting as a significant difference in operability limits is observed. The flashback limit for the smooth injector is at ϕ=0.7, whereas the rough injector can maintain a flame in the combustion chamber until ϕ=0.9. For the high-hydrogen case of 60%, the smooth injector is blow-off resistant and the rough injector is flashback resistant. The 80% hydrogen case has a very small operating range as this type of injector was never designed to run with such high levels of hydrogen. This off-design operating condition makes it harder to stabilize a flame and define the flashback limit at higher equivalence ratio values, but the surface roughness does seem to have a small impact on the blowoff limit. In all cases the smooth injector is more blowoff resistant whereas the rough injector is more flashback resistant.

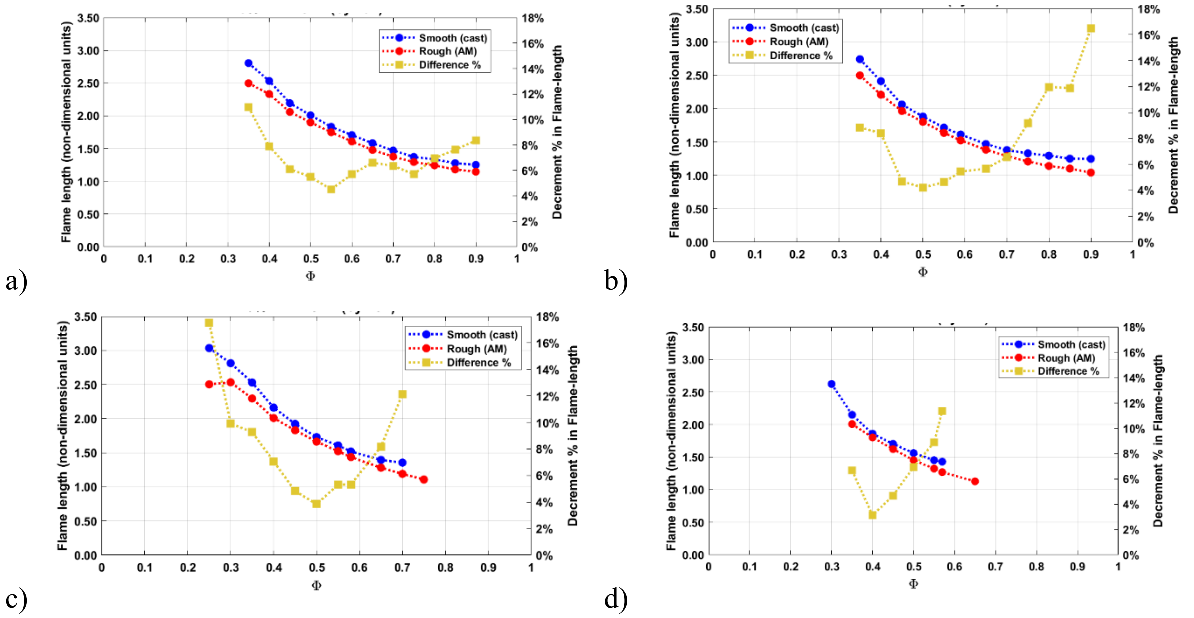

Figure 12. Flame length as a function of equivalence ratio for two surface roughnesses at a) 0% H_2, b) 20% H_2, c) 40% H_2, and d) 60% H_2.

3.4 Design of New Injector Concept Based on DfAM Concepts

In this part of the study, a new injector was designed based off learning from the prior investigations. By incorporating DfAM principles, realizing the benefits of AM, and avoiding some drawbacks of L-PBF, a novel injector design concept arose from two constraints: facilitating additive manufacturing and achieving a wide operability range to facilitate fuel flexibility and turndown. Initial simulations of the injector using large-eddy simulation were completed to understand basic function of the injector. Work regarding both the simulations and experiments for this configuration is on-going.

The injector design integrates novel design features that leverage the design flexibility offered by AM and target enhanced flame stability. The primary objectives of incorporating DfAM guidelines during the design process were to ensure part consolidation, include fixturing considerations, and integrate novel flow features that improve flame stability. A commercial fuel injector for industrial gas turbines typically contains several parts that are separately cast and then brazed or welded for assembly. This arrangement usually widens the manufacturing chain, increases lead times, and makes the process prone to bottlenecks. This L-PBF injector was designed for part consolidation such that the final part would be directly integrated into an existing testing rig [7–9]. The existing test rig setup also provided a volumetric bounding box to contain the design, allowing minimal changes to the setup and direct comparisons with traditionally manufactured designs.

The injector, shown in Figure 13, was designed to run on natural gas and blends of natural gas and hydrogen. As such, a traditional axial swirling configuration with a center pilot was the initial design basis for comparing with prior swirl-stabilized flame experiments. The swirler vanes were designed to provide a swirl number between 0.6 – 0.8, representing swirl numbers seen in most industrial injectors. Additionally, the vane angles were kept at a 55° overhang angle to make them self-supporting for the L-PBF process using IN718 as the material. Another way to stabilize the flame to minimize flashback propensity is to increase the near-wall boundary layer velocity [10]. Considering this, a set of axial and radial air jets are incorporated along the length of the centerbody to improve mixing and increase the near-wall flow velocity, this helps reduce flashback propensity in the near-wall boundary layer of the centerbody. Furthermore, conformal cooling channels are added to reduce the centerbody temperature. The conformal cooling channels exit into the centerbody pilot as tangential jets that impart a counter swirl to the pilot flame with respect to the main flame. In addition to the cooling channels, the centerbody also includes four pairs of thermocouple ports at various distances from the centerbody face to monitor the temperature of the injector wall and its effect on flame anchoring for the various conditions of interest.

The injector design incorporates different fuel delivery strategies to modify flame anchoring and flashback propensity. The fuel for the main flame is delivered through the leading edge of swirler vanes with sufficient distance from the dump plane to premix the fuel and air together. Additionally, the injector has multiple tangential fuel ports at the outlet of the annular passage near the dump plane. This fuel staging can be used to reduce flashback into the swirler region and to modify the flame anchoring by increasing the equivalence ratio of the flow near the outlet of the injector. Finally, the injector includes a centerbody pilot to modify the stability of the flame. The injector incorporates multiple features that would require multiple assembly steps if conventional manufacturing techniques were used. The use of L-PBF enables part consolidation of the injector casing, the swirler, the fuel manifolds and staging ports, the centerbody and pilot lance, and the thermocouple ports.

AM fabrication of the IN718 injector was performed using the 3DSystems ProX 320 L-PBF system; the resulting injector and a cut-away view are shown in Figure 14. Standard recommended processing parameters comprise a 315 W laser power, 100 µm hatch spacing, 65 µm spot size, 1050 mm/s scan speed, and a 60 µm layer thickness for a near-100-percent dense part. The injector was oriented such that the flow direction was printed perpendicular to the build plate. After fabrication and powder removal, the injector was removed from the build plate using wire-EDM. Double-step heat treatment was performed using Homogenization (H) followed by Double Aging (AA) to obtain the high-temperature creep resistance properties for IN718 [11].

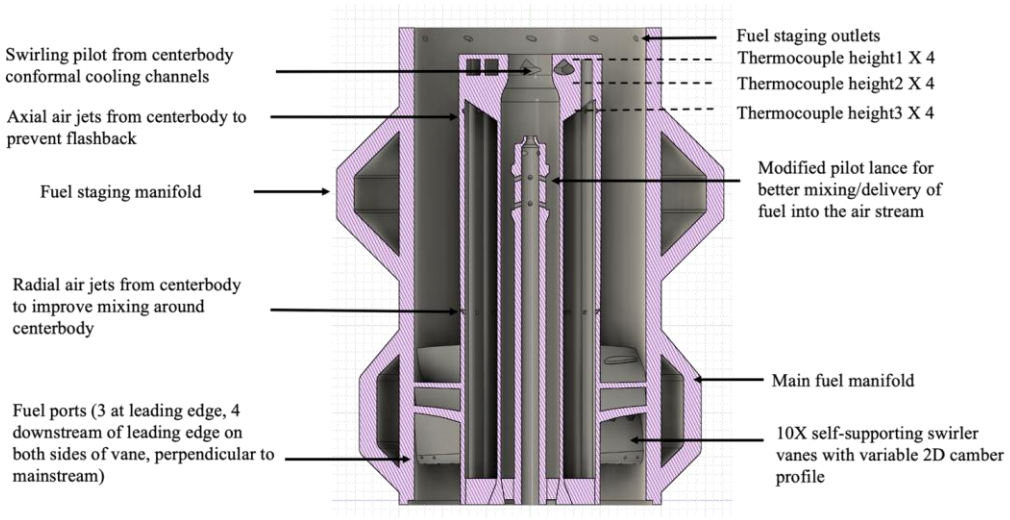

Figure 13. Cross section of the injector with key features called out.

Figure 14. Final printed injector (left) with the cross-sectioned injector (right).

3.5 Injector Simulation and Testing

This work is being prepared for submission for publication; the following section provides an overview of this work. The final publication will be uploaded to OSTI when available.

The optimization method described in Section **Error! Reference source not found.** was used to design several different optimized injectors. Based on the adjoint objective function results of the volume averaged velocity magnitude, the flashback propensity was the highest for the DfAM geometry and the lowest for the Flow optimized. This was expected since the adjoint method optimized the solution to maximize the volume averaged velocity magnitude to obtain the Flow optimized design, thereby ensuring minimum flame flashback propensity. However, the objective function value was lowest for the DfAM design, which indicated that overhang correction tended to redesign against the adjoint optimization. The results of these simulations are shown in Figure 15. The graph represents the velocity magnitude from the near-wall zero velocities to the free-stream velocity in the boundary layer region calculated during the RANS simulations. This velocity build-up was calculated at the tip of the center body which was the flame holding position, and was indicative of flow conditions to assess flashback propensity for non-reacting cases. The velocity build-up was the fastest for the Flow optimized design followed by the DfAM+flow design, the baseline design, and finally the DfAM design.

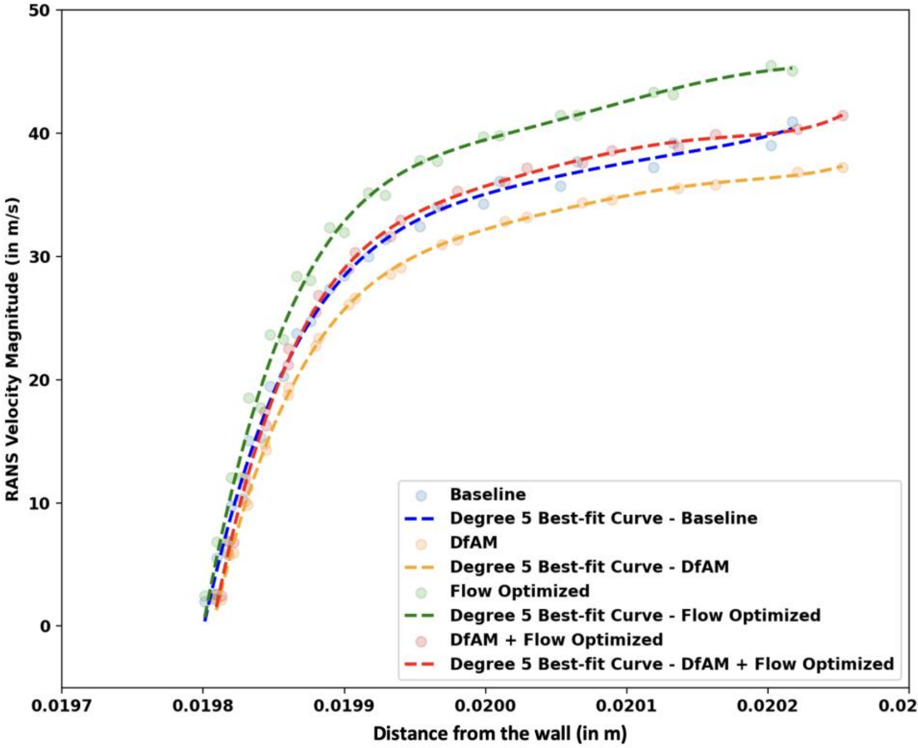

Figure 15: comparison of the near-wall component of the objective function for the different injector designs

To analyze reacting cases, the LES turbulent flame simulations took a total of 30 hours to run using 96 cores. In order to analyze the turbulent flame shapes, the CH* distribution data were time averaged using 2,000 data points for each combination of injector design and fuel composition. The time-averaged CH* distribution plots obtained using simulations for the baseline design were also verified with convoluted time-averaged CH* chemiluminescence experimental results to show consistencies in trends between the pure CH_4 and CH_4 with 40% H_2 configurations therefore verifying the simulation setup. The results are shown in Figure 16. The center of heat release of the flame was impinging less on the combustor walls for the CH_4 with 40% H_2 fuel blend configuration, which was verified with the experimental results. After verifying the simulation setup results for the baseline design with experimental results, the simulation setup was used to analyze the CH* distribution for both fuel conditions for the remaining three designs. These results have been shown in Figure 17. For all the injector designs, the center of heat release impinges lesser on the combustor walls for the 40% H_2 cases. Additionally, the most upstream location within the CH* distribution also significantly varied between injector designs. In order to analyze these differences and correlate it to the flame flashback propensity, the flame contours extracted from the temperature profiles were used.

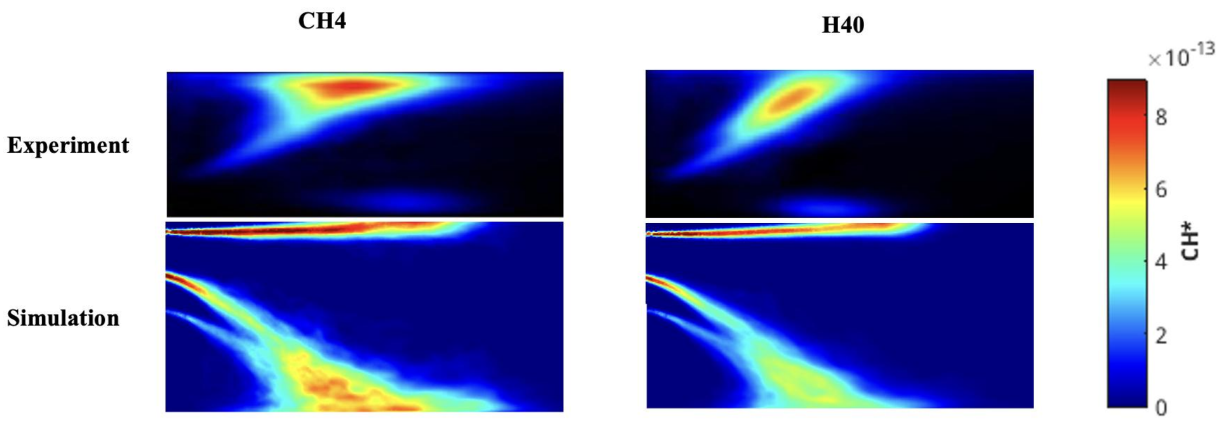

Figure 16: Comparing time-averaged convoluted CH* chemiluminescence images from experiments with the CH* distribution obtained from simulations for the baseline design for CH4 and H40 cases

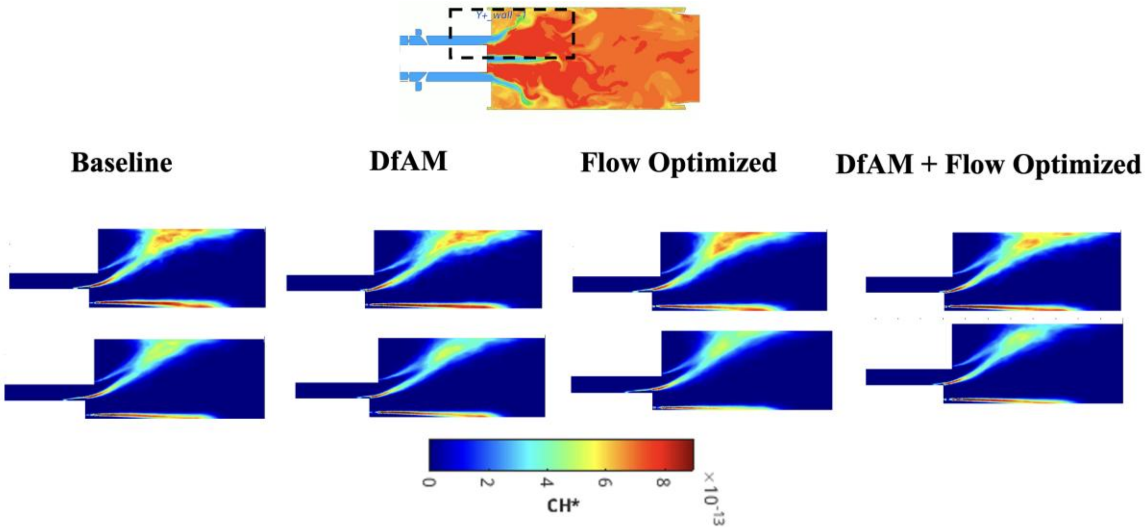

Figure 17: Comparing CH* distribution obtained from simulations for the four design candidates for CH_4 and H40 cases

In order to analyze the flame flashback propensity, the 1000 K mean temperature contour was extracted for all injector design configurations and the most upstream location of this contour provided the flame stabilization location. Based on the adjoint optimization and the non-reacting RANS simulation results, the expected trend for flashback propensity was DfAM > Baseline > DfAM+Flow optimized > Flow optimized due to the opposite trend observed in the objective function of volume averaged velocity magnitude. However, the turbulent flame simulations showed that the flame stabilization location was the most upstream for the Flow optimized injector and the most downstream for the DfAM + Flow optimized injector design. Even when compared to the baseline, the DfAM injector design showed a significantly downstream flame stabilization location. These results were exaggerated for the 40% H_2 fuel composition but maintained the same trend. For all injector designs, the flame stabilized upstream for the 40% H_2 case when compared with the pure CH_4 case. These results have been shown in Figure 18.

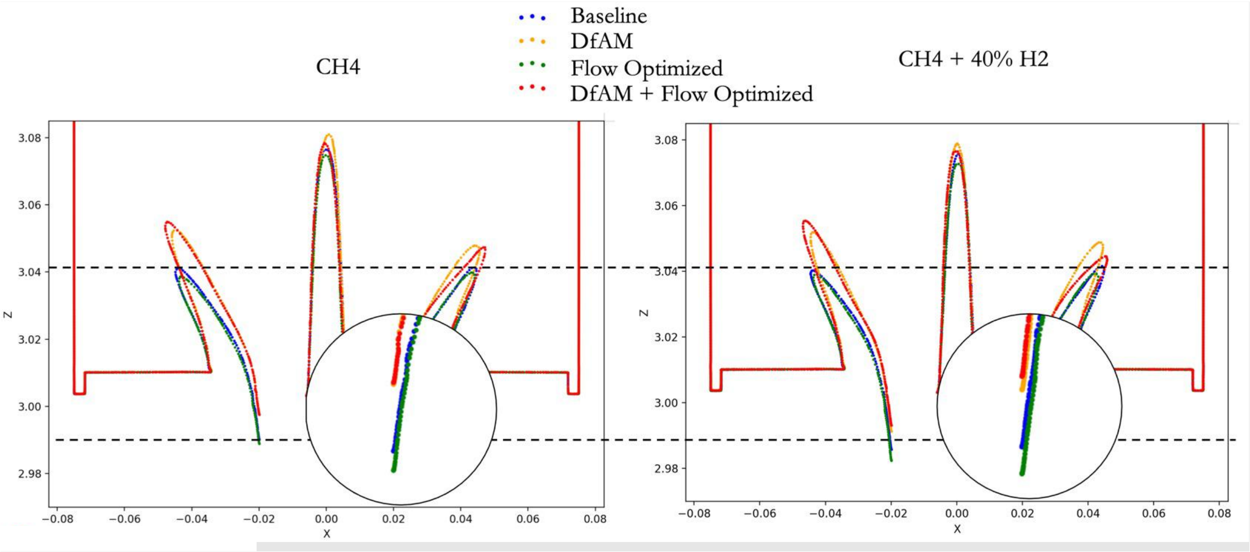

Figure 18: 1000K time averaged ISO contours compared between injector designs for CH4 (left) and 40% H_2 (right) cases

In addition to these results, the shift in flame anchoring location between pure CH_4 and 40% H_2 cases was calculated from their difference in the most upstream location of flame stabilization as a measure of fuel-flexibility for each injector design. It was observed that the shift between the flame stabilization location for both pure CH_4 and 40% H_2 cases for the DfAM+flow optimized design was the least as shown in Figure 19 indicating the highest fuel-flexibility. When compared with the baseline design, the fuel-flexibility of the DfAM+flow optimized design was 62% higher, the DfAM design was 14.99% higher, and the Flow optimized design was -31.83% lower.

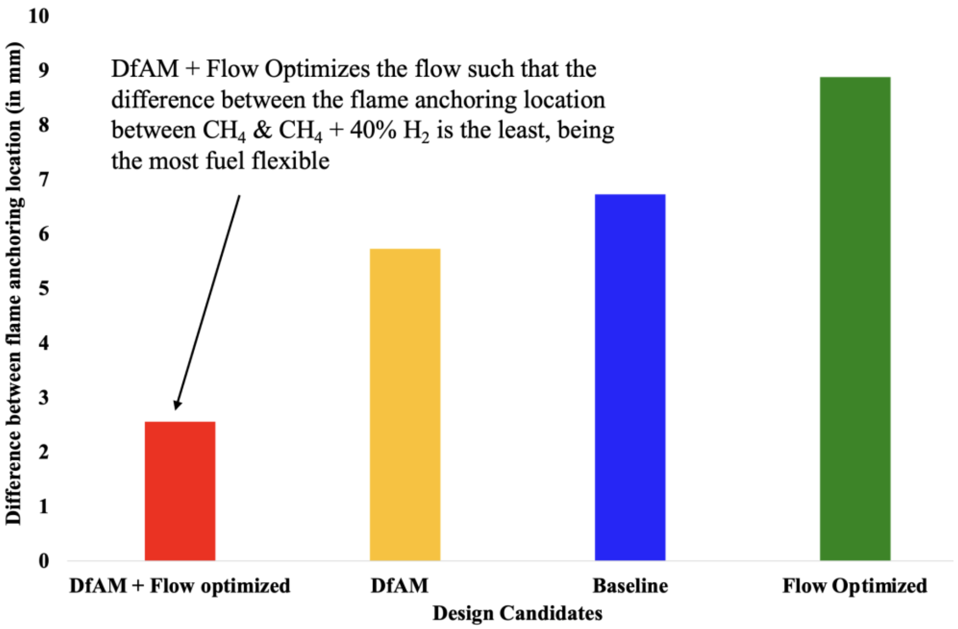

Figure 19: Comparing difference in flame stabilization location between pure CH_4 and CH_4 + 40% H_2 fuel blends for all injector designs

To explain these results, the velocity profiles along the boundary layer development were compared between the baseline and DfAM cases for both RANS and time-averaged LES simulations. For the non-reacting flow cases in RANS used during the adjoint optimization it was found that close to the walls, the velocity magnitude for the baseline was always higher than the DfAM design. However, the axial velocities were higher for the DfAM geometry as compared to the baseline geometry within half the thickness of the turbulent boundary layer. These results are shown in Figure 20.

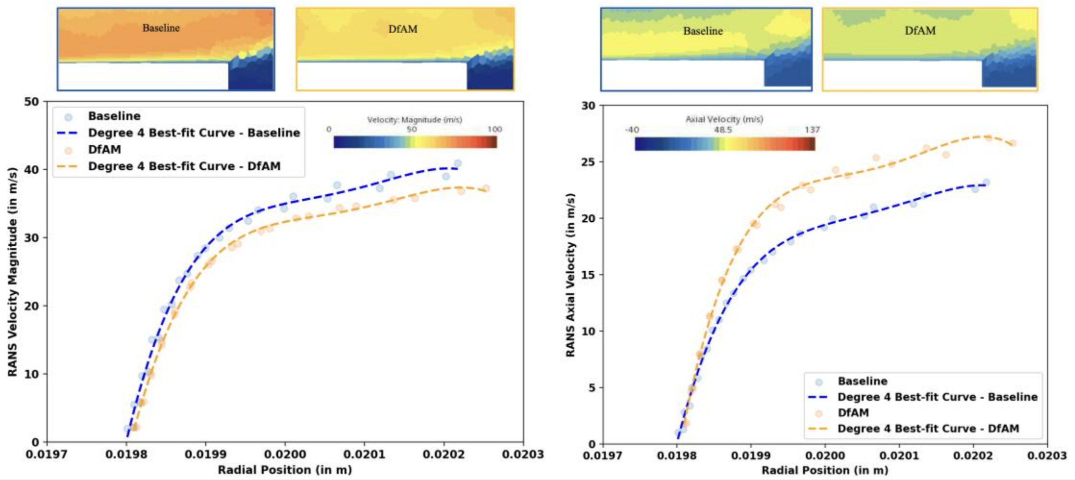

Figure 20: Comparing near-wall velocity magnitude (left) and axial velocities (right) between the baseline and DfAM injector designs

Upon performing similar analysis for near wall time averaged axial velocity comparisons for turbulent reacting time-averaged LES simulations used to compute the flame stabilization location, it was found that the baseline design showed negative velocities in the near-wall region indicating a flow separation as shown in Figure 21. Further investigation of the velocity flow lines overlayed with axial velocity values showed the presence of separation bubbles in case of the baseline. The DfAM geometry however did not show any flow separation. One of the key geometric differences between the flow patterns of the two injector designs was the swirl number, which indicates the ratio between the axial flux of angular momentum to the axial flux of linear momentum [12]. The swirl number at the combustor exit for the baseline geometry was 0.898 whereas it was 0.671 for the DfAM design. Swirl numbers significantly higher than 0.61 have shown to induce flow instabilities that increase the propensity for flame flashback [13].

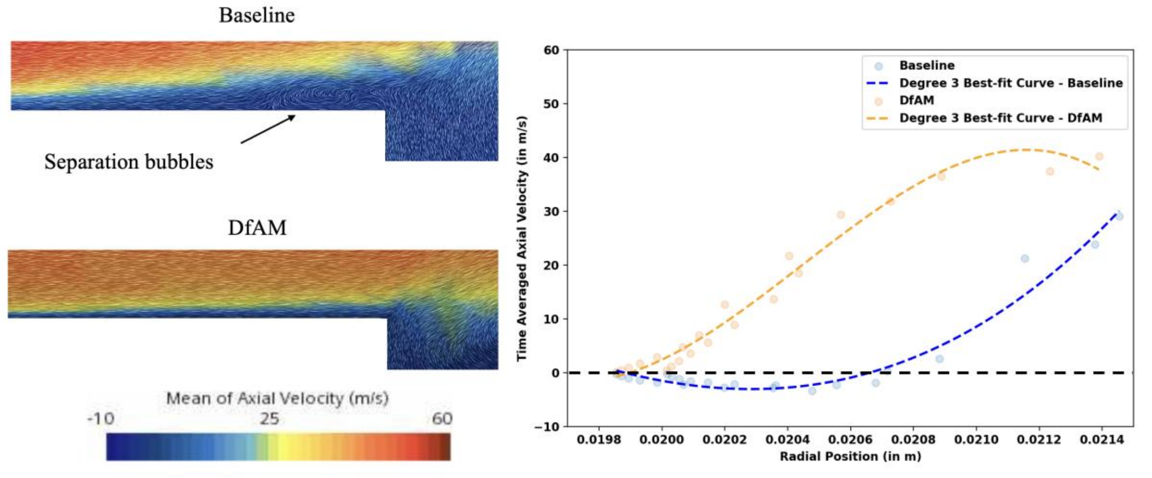

Figure 21: Presence of separation bubbles in the baseline geometry identified using reacting LES simulations

However, this analysis helped in identifying a key limitation of the adjoint method for flow field optimization. Currently, the state of the art commercially available adjoint solvers are compatible only with non-reacting RANS flows. These flow fields do not capture complex features such as the negative flow separation bubbles that are computed in reacting simulations and are exaggerated by the presence of a turbulent flame. Therefore, even though the adjoint optimization maximized the flow field, it exacerbated the complex flow features not being captured in the non-reacting RANS primal solution which resulted in and increased flame flashback propensity. Therefore, the fuel-flexibility performance for the Flow optimized design was the least. On the other hand, for the DfAM geometry, since the complex flow features were not present, the adjoint optimization correctly optimized for flow resulting in a design that is both manufacturable using L-PBF and showed the highest fuel flexible performance by showing the least flame stabilization location shift between different fuel configurations. Experimental testing of these geometries is ongoing. The results of the experimental testing will be reported in the submitted publication.

4 Products

4.1 Students

Students who were funded by this project and their current employers are:

- Dr. Sagar Jalui – PhD student on the project, currently a post-doctoral researcher at Penn State in additive manufacturing
- Pratikshya Mohanty – PhD student on the project, currently a PhD student at Penn State
- Drew Seksinsky – MS student on the project, currently an engineer at KCF Technologies
- Dr. Hyunguk Kwon – PhD student on the project, current an Assistant Professor in the Seoul National University of Science and Technology

4.2 Reports to DOE

O'Connor, J., Manogharan, G., & Xuan, Y. Quarterly Report, October 2024. Development and Evaluation of a Novel Fuel Injector Design Method using Hybrid-Additive Manufacturing. US Department of Energy.

O'Connor, J., Manogharan, G., & Xuan, Y. Quarterly Report, July 2024. Development and Evaluation of a Novel Fuel Injector Design Method using Hybrid-Additive Manufacturing. US Department of Energy.

O'Connor, J., Manogharan, G., & Xuan, Y. Quarterly Report, April 2024. Development and Evaluation of a Novel Fuel Injector Design Method using Hybrid-Additive Manufacturing. US Department of Energy.

O'Connor, J., Manogharan, G., & Xuan, Y. Quarterly Report, January 2024. Development and Evaluation of a Novel Fuel Injector Design Method using Hybrid-Additive Manufacturing. US Department of Energy.

O'Connor, J., Manogharan, G., & Xuan, Y. Quarterly Report, October 2023. Development and Evaluation of a Novel Fuel Injector Design Method using Hybrid-Additive Manufacturing. US Department of Energy.

O'Connor, J., Manogharan, G., & Xuan, Y. Quarterly Report, July 2023. Development and Evaluation of a Novel Fuel Injector Design Method using Hybrid-Additive Manufacturing. US Department of Energy.

O'Connor, J., Manogharan, G., & Xuan, Y. Quarterly Report, April 2023. Development and Evaluation of a Novel Fuel Injector Design Method using Hybrid-Additive Manufacturing. US Department of Energy.

O'Connor, J., Manogharan, G., & Xuan, Y. Quarterly Report, January 2023. Development and Evaluation of a Novel Fuel Injector Design Method using Hybrid-Additive Manufacturing. US Department of Energy.

O'Connor, J., Manogharan, G., & Xuan, Y. Quarterly Report, October 2022. Development and Evaluation of a Novel Fuel Injector Design Method using Hybrid-Additive Manufacturing. US Department of Energy.

O'Connor, J., Manogharan, G., & Xuan, Y. Quarterly Report, July 2022. Development and Evaluation of a Novel Fuel Injector Design Method using Hybrid-Additive Manufacturing. US Department of Energy.

O'Connor, J., Manogharan, G., & Xuan, Y. Quarterly Report, April 2022. Development and Evaluation of a Novel Fuel Injector Design Method using Hybrid-Additive Manufacturing. US Department of Energy.

O'Connor, J., Manogharan, G., & Xuan, Y. Quarterly Report, January 2022. Development and Evaluation of a Novel Fuel Injector Design Method using Hybrid-Additive Manufacturing. US Department of Energy.

O'Connor, J., Manogharan, G., & Xuan, Y. Quarterly Report, October 2021. Development and Evaluation of a Novel Fuel Injector Design Method using Hybrid-Additive Manufacturing. US Department of Energy.

O'Connor, J., Manogharan, G., & Xuan, Y. Quarterly Report, July 2021. Development and Evaluation of a Novel Fuel Injector Design Method using Hybrid-Additive Manufacturing. US Department of Energy.

O'Connor, J., Manogharan, G., & Xuan, Y. Quarterly Report, April 2021. Development and Evaluation of a Novel Fuel Injector Design Method using Hybrid-Additive Manufacturing. US Department of Energy.

O'Connor, J., Manogharan, G., & Xuan, Y. Quarterly Report, January 2021. Development and Evaluation of a Novel Fuel Injector Design Method using Hybrid-Additive Manufacturing. US Department of Energy.

O'Connor, J., Manogharan, G., & Xuan, Y. Quarterly Report, October 2020. Development and Evaluation of a Novel Fuel Injector Design Method using Hybrid-Additive Manufacturing. US Department of Energy.

O'Connor, J., Manogharan, G., & Xuan, Y. Quarterly Report, July 2020. Development and Evaluation of a Novel Fuel Injector Design Method using Hybrid-Additive Manufacturing. US Department of Energy.

O'Connor, J., Manogharan, G., & Xuan, Y. Quarterly Report, April 2020. Development and Evaluation of a Novel Fuel Injector Design Method using Hybrid-Additive Manufacturing. US Department of Energy.

O'Connor, J., Manogharan, G., & Xuan, Y. Quarterly Report, January 2020. Development and Evaluation of a Novel Fuel Injector Design Method using Hybrid-Additive Manufacturing. US Department of Energy.

4.3 Presentations

O'Connor, J., Manogharan, G., & Xuan, Y. (September 24, 2024). "Development and Evaluation of a Novel Fuel Injector Design Method using Hybrid-Additive Manufacturing," 2024 UTSR Project Review Meeting, US Department of Energy, Tuscaloosa, AL.

O'Connor, J., Manogharan, G., & Xuan, Y. (October 30, 2023). "Development and Evaluation of a Novel Fuel Injector Design Method using Hybrid-Additive Manufacturing," 2023 UTSR Project Review Meeting, US Department of Energy, State College, PA.

O'Connor, J., Manogharan, G., & Xuan, Y. (September 29, 2022). "Development and Evaluation of a Novel Fuel Injector Design Method using Hybrid-Additive Manufacturing," 2022 UTSR Project Review Meeting, US Department of Energy, San Diego, CA.

O'Connor, J., Manogharan, G., & Xuan, Y. (November 9, 2021). "Development and Evaluation of a Novel Fuel Injector Design Method using Hybrid-Additive Manufacturing," 2021 UTSR Project Review Meeting, US Department of Energy, Online.

O'Connor, J., Manogharan, G., & Xuan, Y. (November 18, 2020). "Development and Evaluation of a Novel Fuel Injector Design Method using Hybrid-Additive Manufacturing," 2020 UTSR Project Review Meeting, US Department of Energy, Online.

O'Connor, J., Manogharan, G., & Xuan, Y. (November 7, 2019). "Development and Evaluation of a Novel Fuel Injector Design Method using Hybrid-Additive Manufacturing," 2019 UTSR Project Review Meeting, US Department of Energy, Orlando, FL.

4.4 Papers (published)

- Li, J., Kwon, H., Seksinsky, D., Doleiden, D., O'Connor, J., Xuan, Y., Akiki, M. and Blust, J., (2022) "Describing the Mechanism of Instability Suppression Using a Central Pilot Flame With Coupled Experiments and Simulations," *Journal of Engineering for Gas Turbines and Power*, 144(1), p. 011015.
- O'Connor, J. (2023). Understanding the role of flow dynamics in thermoacoustic combustion instability. *Proceedings of the Combustion Institute*, 39(4), 4583-4610.
- Jalui, S. S., Spurgeon, T. J., Jacobs, E. R., Chatterjee, A., Stecko, T., and Manogharan, G. P., (2021) "Abrasive Flow Machining of Additively Manufactured Titanium: Thin Walls and Internal Channels," Proceedings of Solid Freeform Fabrication Symposium 2021.
- Jalui, S., Xuan, Y., Manogharan, G., & O'Connor, J. (2025). Development of a Method for Shape Optimization for a Gas Turbine Fuel Injector Design Using Metal-Additive Manufacturing. *Journal of Engineering for Gas Turbines and Power*, 147(1), p. 011023.
- Mohanty, P., Jalui, S., Manogharan, G., O'Connor, J., Xuan, Y. (2024) "Flashback characterization of additively manufactured swirl-stabilized fuel injector with varying surface roughness." *Spring Technical Meeting of the Eastern State Section of the Combustion Institute,* Athens, GA.

4.5 Outreach

Featured in *The Cool Parts Show*, a web video series published by Additive Manucturing Media

- https://www.youtube.com/watch?v=no_7eZe-Muo
- https://www.youtube.com/watch?v=B9ScUHspMQs

Incorporated additive manufacturing and design optimation into two summer undergraduate research experiences:

- Summer Research Experience for Undergrads hosted by Penn State Center for Gas Turbine Research, Education, and Outreach (GTREO) and Center For Innovative Materials Processing Through Direct Digital Deposition (CIMP-3D) on additive manufacturing for fuel injectors
- NSF REU (PIs: J. O'Connor and K. Thole, grant EEC-2149667) with projects focused on thermoacoustics, design optimization, computer simulation, and additive manufacturing, https://sites.psu.edu/powerpropulsionreu/

Incorporated components of the project into two courses:

- ME 556: Design for Additive Manufacturing (graduate level) – two teams design challenge for gas turbine swirler design to enhance lean blow-off limits
- ME 404: Gas Turbines (undergraduate level) – case study on additive manufacturing for fuel injectors in gas turbine engines

5 References

[1] Li, J., Kwon, H., Seksinsky, D., Doleiden, D., Xuan, Y., O'Connor, J., Akiki, M., and Blust, J., 2021, "Describing the Mechanism of Instability Suppression Using a Central Pilot Flame with Coupled Experiments and Simulations," J Eng Gas Turbine Power, **144**(1), p. 011015.

[2] Zimont, V., Polifke, W., Bettelini, M., and Weisenstein, W., 1997, *An Efficient Computational Model for Premixed Turbulent Combustion at High Reynolds Numbers Based on a Turbulent Flame Speed Closure*, American Society of Mechanical Engineers.

[3] Lieuwen, T. C., and Yang, V., 2005, *Combustion Instabilities in Gas Turbine Engines: Operational Experience, Fundamental Mechanisms, and Modeling*, American Institute of Aeronautics and Astronautics, Reston, VA.

[4] McDonell, V., 2016, "Lean Combustion in Gas Turbines," *Lean Combustion*, D. Dunn-Rankin, and P. Therkelsen, eds., Academic Press, London, UK, pp. 147–201.

[5] Li, J., Peluso, S., Quay, B., Santavicca, D., Blust, J., and Srinivasan, R., 2017, "Effect of Pilot Flame on Flame Macrostructure and Combustion Instability," *Turbo Expo: Power for Land, Sea, and Air*, Charlotte, NC.

[6] Aupoix, B., 2015, "Roughness Corrections for the k–ω Shear Stress Transport Model: Status and Proposals," J Fluids Eng, **137**(2), p. 021202.

[7] Camacho, J. R., Akiki, M., Blust, J., and O'Connor, J., 2024, "Effect of Inert Species on the Static and Dynamic Stability of a Piloted, Swirl-Stabilized Flame," J Eng Gas Turbine Power, **146**(6). https://doi.org/10.1115/1.4064048.

[8] Doleiden, D., Karmarkar, A., O'connor, J., and Blust, J., 2022, "IMPACT OF CENTRAL PILOTING ON THE STATIC AND DYNAMIC STABILITY OF SWIRL-STABILIZED FLAMES," *Proceedings of ASME Turbo Expo 2022 Turbomachinery Technical Conference and Exposition*, Rotterdam, The Netherlands. [Online]. Available: http://asmedigitalcollection.asme.org/GT/proceedings-pdf/GT2022/85994/V03AT04A016/6935065/v03at04a016-gt2022-80226.pdf.

[9] Li, J., Kwon, H., Seksinsky, D., Doleiden, D., O'Connor, J., Xuan, Y., Akiki, M., and Blust, J., 2022, "Describing the Mechanism of Instability Suppression Using a Central Pilot Flame With Coupled Experiments and Simulations," J Eng Gas Turbine Power, **144**(1). https://doi.org/10.1115/1.4052384.

[10] Jalui, S., Xuan, Y., Manogharan, G., and O'Connor, J., 2025, "Development of a Method for Shape Optimization for a Gas Turbine Fuel Injector Design Using Metal-Additive Manufacturing," J Eng Gas Turbine Power, **147**(1). https://doi.org/10.1115/1.4066509.

[11] Huang, W., Yang, J., Yang, H., Jing, G., Wang, Z., and Zeng, X., 2019, "Heat Treatment of Inconel 718 Produced by Selective Laser Melting: Microstructure and Mechanical Properties," Materials Science and Engineering: A, **750**, pp. 98–107. https://doi.org/10.1016/J.MSEA.2019.02.046.

[12] Faeth, G. M., 1986, "Swirl Flows: A. K. Gupta, D. G. Lilley, and N. Syred, Abacus Press, Tunbridge Wells, England, 1984, Xiii + 475 Pp, $50.00," Combust Flame, **63**(1), p. 311. https://doi.org/https://doi.org/10.1016/0010-2180(86)90133-1.

[13] Manoharan, K., Frederick, M., Clees, S., O'Connor, J., and Hemchandra, S., 2019, "A Weakly Nonlinear Analysis of the Precessing Vortex Core Oscillation in a Variable Swirl Turbulent Round Jet," J Fluid Mech, **884**, p. A29. https://doi.org/10.1017/jfm.2019.903.